JOURNAL OF AIRCRAFT
Vol. 31, No. 1, Jan.–Feb. 1994

Measurement of Unsteady Airloads on an Oscillating Engine and a Wing/Engine Combination

H. Triebstein* and G. Schewe*
DLR Institute of Aeroelasticity, Göttingen, Germany
and
H. Zingel† and S. Vogel†
Deutsche Airbus GmbH, Bremen 1, Germany

Experimental investigations of unsteady aerodynamic forces were performed on an oscillating ejector engine model and a wing/engine combination in the subsonic and transonic flow regimes. The experimental results were compared with theoretical results. The aim was to determine how well, in reality, the mathematical aerodynamic models commonly used for flutter calculations correspond to the flow conditions on an engine. The investigations on the isolated ejector engine demonstrated that linear lifting surface theory provides quite accurate unsteady aerodynamic forces. The effects of the Mach number and reduced frequency are described correctly. For the wing/engine combination, the unsteady interference effect of the engine oscillation on the lower side of the wing is strongly influenced by flow separation at the wing/pylon connection. In general, the unsteady aerodynamic forces induced by the engine on the wing are small and are therefore of minor influence on the unsteady airloads of an oscillating wing.

Nomenclature

A = cross-sectional area, m^2
a = speed of sound, m/s
c_M = pitch moment coefficient
c_m = local pitch moment coefficient referred to $l/4$
c_N = normal force coefficient
c_n = local normal force coefficient
c_p = pressure coefficient
c_p^* = critical pressure coefficient
d = engine inlet diameter, m
f = frequency, Hz
Im = imaginary part of complex quantity
l = nacelle length, local chord, m
l_μ = reference chord, m
M = pitch moment, Nm
M_∞ = freestream Mach number
$\dot{m}$ = mass flow, kg/s
N = normal force, N
p = static pressure, Pa
p_t = engine model driving pressure, Pa
q = dynamic pressure, Pa
Re = Reynolds number
Re = real part of complex quantity
S = wing area, m^2
U_∞ = freestream velocity, m/s
x, y, z = Cartesian coordinates, parallel to the fuselage, m
$\bar{x}, \bar{y}, \bar{z}$ = Cartesian coordinates, parallel to the fuselage (opposite sign), m
$\tilde{x}, \tilde{y}, \tilde{z}$ = Cartesian coordinates, swept, m
α = angle of incidence
γ = damping ratio
Δc_p = pressure difference $c_{p,\text{lower}} - c_{p,\text{upper}}$
ζ = mass flow coefficient
Λ = aspect ratio
λ = taper ratio
ν = kinematic viscosity, m^2/s
ρ = density, kg/m
φ_{25} = sweep angle of $l/4$ line
ω = circular frequency, 1/s
ω^* = reduced frequency

Subscripts
lower = lower surface
upper = upper surface
α = quasisteady quantity
∞ = freestream conditions
1 = engine pressure supply
2 = engine inlet cross section
5 = engine exhaust nozzle cross section

Introduction

TO improve the efficiency of aircraft engines and reduce noise emission, the bypass ratio of the engines has been increased in the past and will be further increased in the future. Aircraft engines of the future, e.g., the projected General Electric GE 90 or the counter rotating integrated shrouded propeller (CRISP) project, will have a bypass ratio of 10–20. High bypass ratio engines result in a large engine diameter.

Flutter calculations on aircraft with two large engines located far in front of the wing leading edge, e.g., as performed by Zimmermann and Vogel,[1] have shown that above the wing bending frequency an engine pitch mode with a significant torsion of the wing exists (Fig. 1). With increasing airspeed the frequencies of these two vibration modes come closer together, the damping curve passes the zero line, and flutter instability occurs. Figure 1 also shows the influence of the engine airloads on the flutter behavior. The engine airloads reduce the generalized stiffness of the vibration modes with engine vibration constituents, by which the frequencies become lower with increasing airspeed. The damping of the vibration modes with engine vibration constituents is increas-

Presented as Paper 90-3.1.1 at the 17th Congress of the International Council of the Aeronautical Sciences, Stockholm, Sweden, Sept. 9–14, 1990; received Nov. 19, 1991; revision received May 11, 1992; accepted for publication Oct. 30, 1992.

*Research Scientist, German Aerospace Research Establishment, D-3400, Bunsenstraße 10.

†Development Engineer, Department for Aeroelasticity, Postfach 10 78 45, 2800.

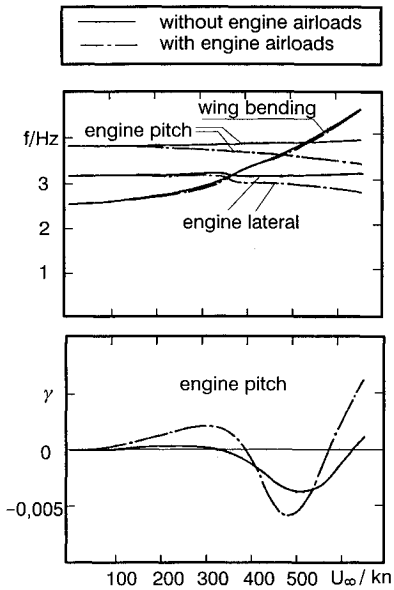

Fig. 1 Influence of the airloads of the engine on the f and γ of basic modes.[1]

ing. The coupling terms of the generalized airloads are increased, by which the loss of damping is increased. The sum of these effects leads to a stronger flutter situation and to a flutter point at higher airspeed.

In the present method of calculating the airloads on the engine, the nacelle is modeled as a circular cylinder with zero wall thickness.[2,3] Not represented by this procedure are 1) the nacelle profile; 2) the cowling geometry; 3) nonlinear interference effects due to flow separation in the junction between engine, pylon, and wing; 4) the fan jet; and 5) the primary jet.

Wind-tunnel tests were performed on an isolated engine model in the Göttingen 3 × 3 m² low speed wind tunnel and in the ONERA S2 transonic wind tunnel in Modane, as well as on a wing/engine combination in the Göttingen 3 × 3 m² low speed wind tunnel. The aim was to determine how well the mathematical aerodynamic models commonly used for flutter calculations correspond to the flow conditions around engines and wing/engine combinations in reality. This article gives a summary of the results. Some more details are discussed in other publications.[4,5]

Experimental Investigations on the Isolated Engine Model

The state-of-the-art of engine simulation in wind tunnels are the turbine powered simulator (TPS) models, by which the aerodynamic parameters such as the inlet mass flow coefficient and the exhaust nozzle impulse are well approximated. However, the TPS models are very sensitive to vibrations and thus cannot be used for investigations on harmonically oscillating engine models. Therefore, the ejector principle was used for jet simulation in our tests.

The wind-tunnel model and the principle of the test arrangement are shown in Fig. 2. The engine model is a 1:13 scaled General Electric CF6-50 engine. Pressurized air ($\dot{m}_1$) is led into the engine model with a pressure of up to 20 bar, and is blown out through Laval nozzles. The pressurized air entering the bypass channel sweeps along with it the air entering the engine through the inlet, thus increasing the mass flow through the inlet $\dot{m}_2$. The mass flow at the bypass exhaust nozzle becomes

$$\dot{m}_5 = \dot{m}_1 + \dot{m}_2 \tag{1}$$

The engine model is fixed by a sting in an electrohydraulic actuator and can be driven to harmonic pitch vibrations. The model is instrumented with a piezoelectric balance, which is mounted between the sting and engine. The outstanding property of such a piezo balance is its high stiffness, which is a prerequisite for the unsteady measurements. Details concerning the balance that is integrated in the engine are given by Schewe.[6,7] A total of 33 pressure transducers are mounted in three nacelle sections (see Fig. 2). Four accelerometers and a rotation angle pickup measure the engine model vibrations.

To determine the mass flows through the engine model, calibration measurements were performed in the Göttingen calibration tank. Figure 3 shows the dimensionless mass flow coefficients

$$\zeta_2 = \dot{m}_2/(\rho_\infty a_\infty M_\infty A_2) \tag{2a}$$

at the engine inlet and

$$\zeta_5 = \dot{m}_5/(\rho_\infty a_\infty M_\infty A_2) \tag{2b}$$

at the exhaust nozzle vs M_∞ and for different driving pressures p_t. With increasing Mach number, the effectiveness of the ejector decreases. At $M_\infty > 0.6$, the inlet mass flow can no longer be increased by increasing driving pressure. While ζ_2 of the aircraft is not reached for low Mach numbers, and is crudely approximated for cruise conditions, the exhaust nozzle ζ_5 is well approximated.

Figure 4 shows the measured pressure distribution

$$c_p(x/l) = [p(x/l) - p_\infty]/q_\infty \tag{3}$$

of section 2 for different mass flow coefficients ζ_2 and ζ_5, and for different M_∞. The pressure distributions of the undriven engine ($p_t = 1$ bar) at subsonic $M_\infty < 0.8$ are characterized by a suction peak at the nacelle leading edge. A second, smaller suction peak at $x/l = 0.2$ is caused by a discontinuity of the nacelle profile. The pressures on the nacelle inner side

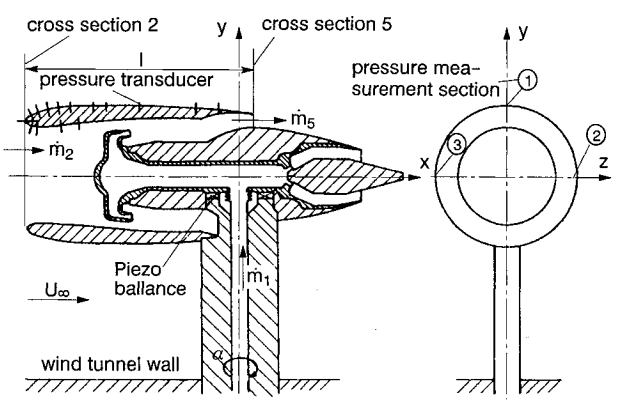

Fig. 2 Engine model.

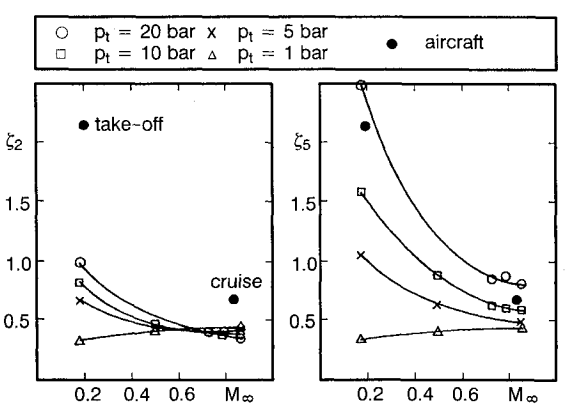

Fig. 3 Influence of M_∞ on ζ_2 and ζ_5.

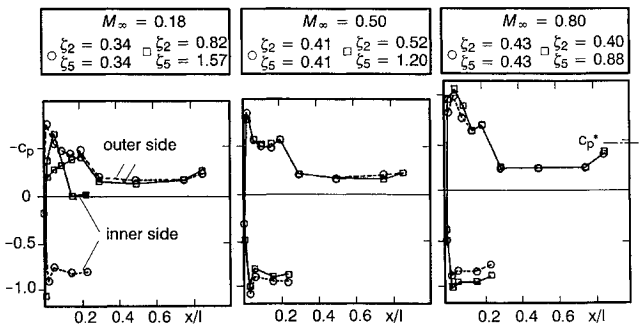

Fig. 4 Steady pressure distribution $c_p(x/l)$; influence of M_∞ and ζ_2 and ζ_5; α = 0 deg; section 2.

are relatively high. This is due to the throttling caused by the necessary installations in the bypass channel.

The increase in the Mach number from $M_\infty = 0.18$ to $M_\infty = 0.5$, leads to only a small increase in the suction peaks on the nacelle outer side, and to an increase in the pressures on the inner side. At $M_\infty = 0.8$, supersonic flow locally occurs, indicated by pressure coefficients larger than c_p^*.

The increase of the inlet ζ_2 at low $M_\infty = 0.18$ results in a shift of the stagnation point on the inner side of the nacelle towards the leading edge. Consequently, the suction peak on the outer engine side is decreased, and a suction peak on the inner side is now built-up.

At higher $M_\infty = 0.5$, ζ_2 is nearly unchanged with increasing driving pressure. The pressure distribution is only slightly influenced on the inner side of the nacelle; the increasing exhaust nozzle mass flow hardly affects the pressure distribution of the nacelle.

At the transonic $M_\infty = 0.8$, the increasing driving pressure causes a stronger throttling of the through-flow. This results in a pressure increase on the nacelle inner side and a slight change of the supersonic flow region.

The quasisteady normal force coefficient

$$c_{N,\alpha} = [c_N(\alpha_1) - c_N(\alpha_2)]/(\alpha_1 - \alpha_2) = N_\alpha/(q_\infty d_2 l) \tag{4}$$

and the quasisteady pitch moment coefficient

$$c_{M,\alpha} = [c_M(\alpha_1) - c_M(\alpha_2)]/(\alpha_1 - \alpha_2) = M_\alpha/(q_\infty d_2 l^2) \tag{5}$$

were calculated with a steady panel method based on potential flow theory.[8] They are plotted in Fig. 5 vs ζ_2. This calculation method[8] is able to consider the nacelle profile, the inlet mass flow, and the exhaust nozzle mass flow separately, as well as the jet.

With increasing ζ_2, $c_{N,\alpha}$, and $c_{M,\alpha}$ are increasing linearly. A systematic change of ζ_5 results in the assessment that this parameter does not significantly affect the engine airloads. $c_{N,\alpha}$ and $c_{M,\alpha}$ were calculated with the doublet-lattice method,[2] and the engine model was idealized by an approximated circular cylinder. The calculated values are somewhat smaller than the values calculated with the steady panel method.[8] A reason for this difference could be the simplified engine geometry in the doublet-lattice calculation.

The measured pressure distributions were integrated to obtain $c_{N,\alpha}$ and $c_{M,\alpha}$. The calculation was based on the cross section 2 only. The pressure distribution in the circumferential direction was approximated by a simple cosine distribution. The agreement between measurement and calculation is good.

Taking into account the interference effect of the engine sting in the doublet-lattice calculation, predominantly results in a higher normal force slope. The force measurement, done by using the piezo balance and including the interference effect, gives corresponding larger quasisteady normal force

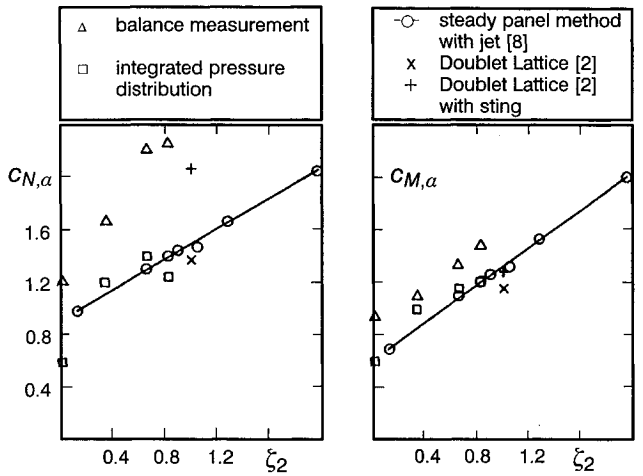

Fig. 5 Quasisteady normal force and pitch moment coefficients $c_{N,\alpha}$ and $c_{M,\alpha}$, respectively, depending on ζ_2; M_∞ = 0.18.

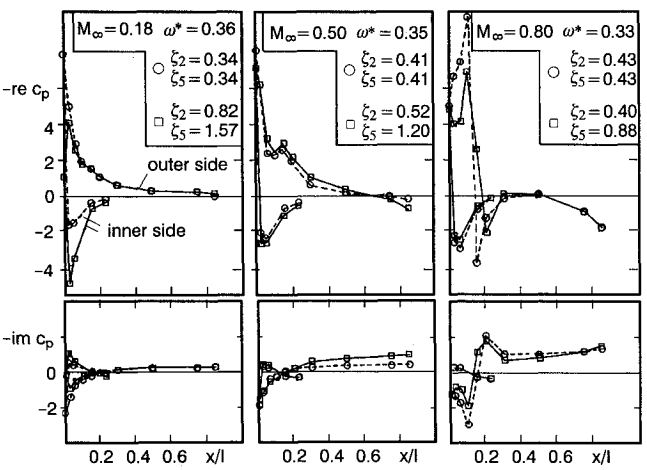

Fig. 6 Influence of M_∞ on the unsteady pressure distribution Re $c_p(x/l)$ and Im $c_p(x/l)$ of the engine; α = 0 deg; section 2.

and pitch moment coefficients than the integrated pressure distribution does.

The unsteady airloads were measured on the harmonically pitching engine model. The unsteady pressure distributions

$$\text{Re } c_p(x/l) + i \text{ Im } c_p(x/l) = \text{Re } p(x/l)/q_\infty + i \text{ Im } p(x/l)/q_\infty \tag{6}$$

are plotted in Fig. 6 for different M_∞ and the different ζ_2 and ζ_5. At subsonic $M_\infty = 0.18$ and $M_\infty = 0.5$, the unsteady pressure distributions are characterized by a marked suction peak near the nacelle leading edge on the outer side. With the increasing ζ_2, the pressure peak on the inner side of the nacelle increases, whereas the suction peak on the outer side decreases. With increasing Mach number the pressure peak on the inner side increases, but this also is an effect of the increased ζ_2. At the transonic $M_\infty = 0.8$, a pronounced suction peak occurs at $x/l = 0.1$, which corresponds to the maximum pressure slope $\partial c_p/\partial x$ of the steady pressure distribution (Fig. 4). In the supersonic region, the flow is sensitive to small changes of the mass flow parameters ζ_2 and ζ_5.

The unsteady pressure distributions were integrated in the same way as the steady pressure distributions in order to obtain $c_{N,\alpha}$ and $c_{M,\alpha}$, which are plotted in Fig. 7 vs the reduced frequency:

$$\omega^* = 2\pi f l/U_\infty \tag{7}$$

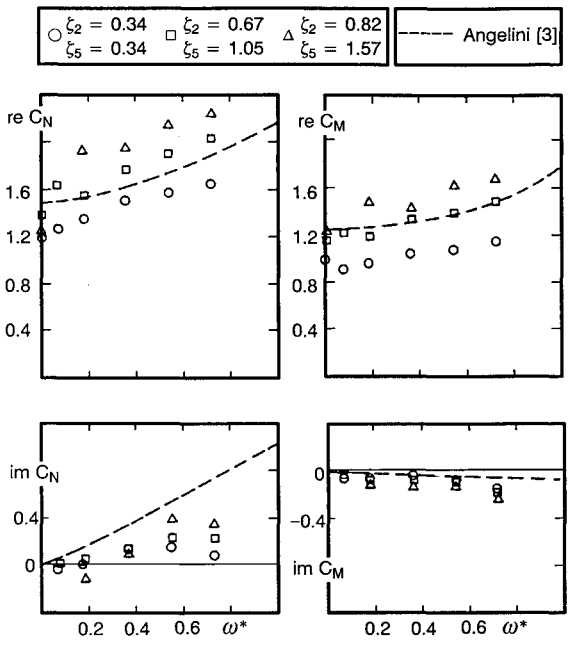

Fig. 7 Unsteady normal force coefficients Re c_N and Im c_N and pitch moment coefficients Re c_M and Im c_M vs ω^*; influence of ζ_2 and ζ_5; $M_\infty = 0.18$.

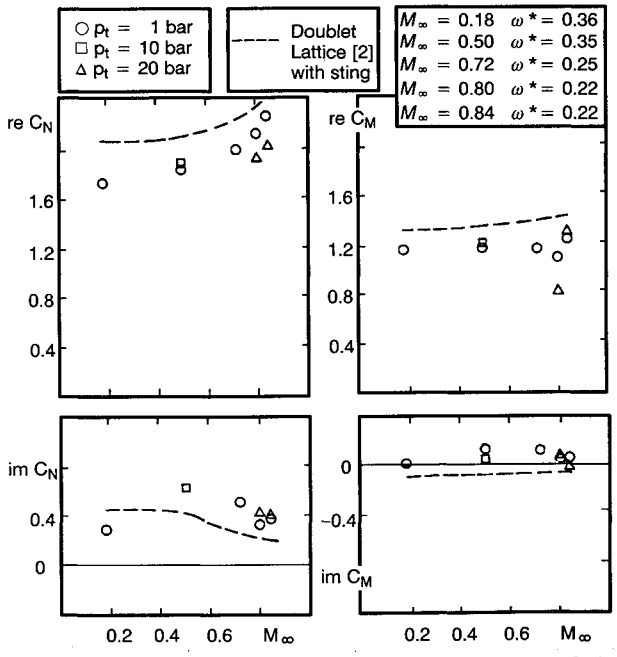

Fig. 8 Unsteady normal force coefficients Re c_N and Im c_N and pitch moment coefficients Re c_M and Im c_M vs M_∞; $\zeta_2 \approx 0.4$.

The tests were performed at $M_\infty = 0.18$ for different ζ_2 and ζ_5. The measurements show that with increasing ω^*, the real parts of the normal force coefficient and the pitch moment coefficient increase slightly. It is further evident that with increasing mass flow coefficients the normal force and pitch moment coefficients also increase in the real and imaginary parts.

The unsteady airloads of the engine model were calculated using a kernel function method of Angelini.[3] The engine model geometry was approximated by a through-flow nacelle that has the shape of a circular cylinder (mass flow parameters ($\zeta_2 = \zeta_5 = 1$). Comparison of the measurements and calculations shows that the increase in the real parts with increasing reduced frequency are well approximated. However, the values of the real parts are underpredicted if compared to extrapolation of the measurements to $\zeta_2 = 1$.

The influence of M_∞ on the unsteady normal force and pitch moment coefficients is plotted in Fig. 8. In this case, the forces and moments were measured using the piezo balance. The inlet mass flow coefficient is approximately constant ($\zeta_2 = 0.4$), while the exhaust nozzle mass flow coefficient changes with increasing p_t. With increasing Mach number, the real part of the normal force coefficient is slightly increasing. The real part of the pitch moment coefficient is nearly constant, but the measured values show a certain scatter at transonic Mach numbers.

The unsteady airloads were calculated using the doublet-lattice method. The interference of the sting is included in the calculation, and the Mach number dependency on the unsteady airloads is well approximated by the calculation. The calculated unsteady airloads are higher than the measured ones, because the calculation was performed with the larger inlet mass flow coefficient $\zeta_2 = 1$.

Experimental Investigations on the Wing/Engine Combination

After the steady and unsteady airloads had been investigated on the isolated engine, the influence of the wing on the engine airloads and vice versa were studied.

The test arrangement in the Göttingen 3 × 3 m² low speed wind tunnel is shown in Fig. 9. The engine can be driven to harmonic pitch vibrations with an electrohydraulic actuator, whereas the wing is at rest.

The instrumentation of the engine model was nearly the same as for the measurements on the isolated engine. The wing was instrumented with a total of 120 pressure transducers in four sections, and six accelerometers. For measurement of the steady and unsteady forces on the wing, a second balance based on piezoelectric multicomponent force transducers was installed at the root of the wing. This balance and further results are described by Schewe.[7]

In Fig. 10 the steady pressure distributions $c_p(x/l)$ on the wing are plotted for different ζ_2 and ζ_5. For all mass flow coefficients it can be noticed that the stagnation point is shifted towards the wing leading edge, passing the sections from the root towards the tip. Due to the influence of increasing jet strength ζ_5, the stagnation point is shifted towards the leading edge in the sections considered. This results in a decrease in the suction on the wing's upper side. Simultaneously, the suction increases on the lower side. The total result is a decrease of c_N of the wing, and an increase of the nose-heavy

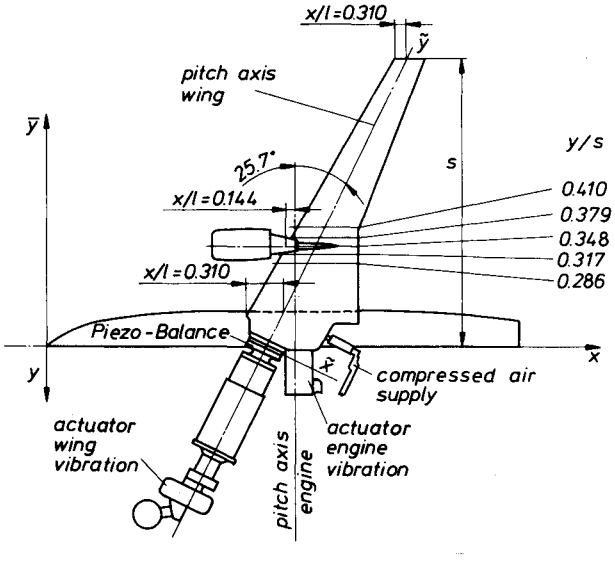

Fig. 9 Test arrangement of the wing/engine combination ($s = 1.697$ m, $S = 0.648$ m², $l_\mu = 0.380$ m, $\Lambda = 8.8$, $\lambda = 0.26$, $\varphi_{25} = 28$ deg).

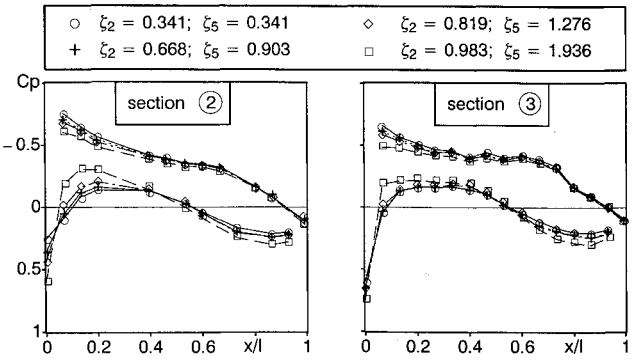

Fig. 10 Steady pressure distribution $c_p(x/l)$ of the wing, influence of the jet strength ζ_5; $M_\infty = 0.18$; $\alpha = 3$ deg.

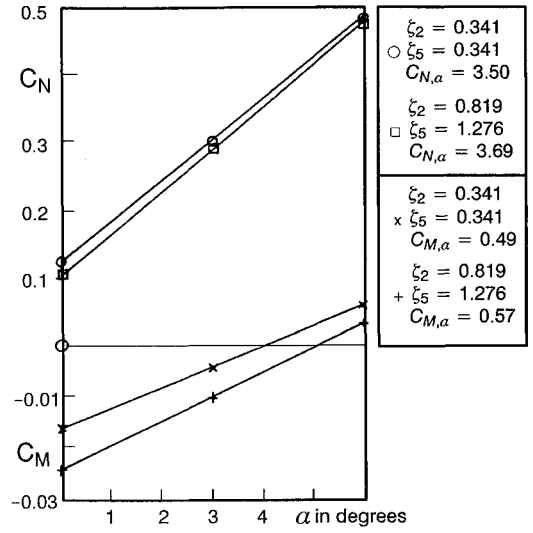

Fig. 11 Steady normal force and pitch moment coefficients $c_N(\alpha)$ and $c_M(\alpha)$, respectively; influence of jet strength ζ_5; $M_\infty = 0.18$.

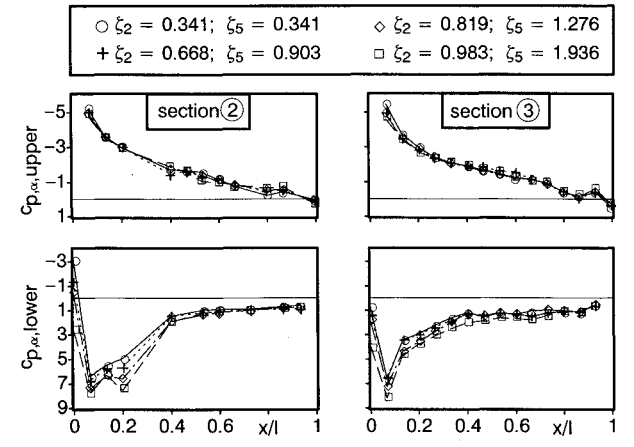

Fig. 12 Quasisteady pressure distribution $c_{p,\alpha}(x/l)$ of the wing, influence of the jet strength ζ_5; $M_\infty = 0.18$; $\alpha = 0$ deg; $\dot{\alpha} = 0.5$ deg.

c_M, as is plotted in Fig. 11. The normal force coefficient of the wing is defined as

$$c_N = N/(q_\infty S) \tag{8}$$

The pitch moment coefficient referred to the pitch axis is defined as

$$c_M = M/(q_\infty S l_\mu) \tag{9}$$

The influence of the engine on the quasisteady pressure distribution of the wing

$$c_{p,\alpha}(x/l) = \frac{[c_p(x/l, \alpha_1) - c_p(x/l, \alpha_2)]}{(\alpha_1 - \alpha_2)} \tag{10}$$

is shown in Fig. 12. Due to the influence of the jet strength ζ_5, the quasisteady pressure on the lower surface increases significantly, while the quasisteady pressure distribution on the upper surface remains nearly unaffected. This results in an increase of the local quasisteady normal force coefficient $c_{n,\alpha}(\bar{y}/s)$, and an increase of the local tail-heavy pitch moment coefficient $c_{m,\alpha}(\bar{y}/s)$, with increasing ζ_5, as plotted in Fig. 13. Comparison of the measurement with a doublet-lattice calculation shows good agreement.

The unsteady pressure distributions Re $c_p(x/l)$ and Im $c_p(x/l)$ of the wing at rest, due to the oscillating engine, are plotted in Fig. 14 for two sections and at different ω^*. The unsteady pressure distribution on the lower surface differs remarkably from that on the upper surface. Pronounced minima and maxima are found at different locations inboard and outboard of the pylon. The wave character of the unsteady

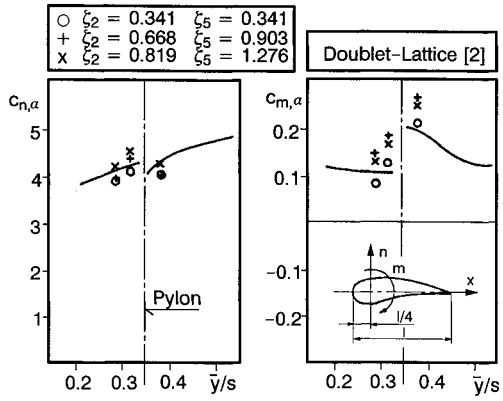

Fig. 13 Quasisteady normal force and pitch moment coefficients $c_{n,\alpha}(\bar{y}/s)$ and $c_{m,\alpha}(\bar{y}/s)$, respectively; influence of the jet strength ζ_5; $M_\infty = 0.18$; $\alpha = 0$ deg; $\dot{\alpha} = 0.5$ deg.

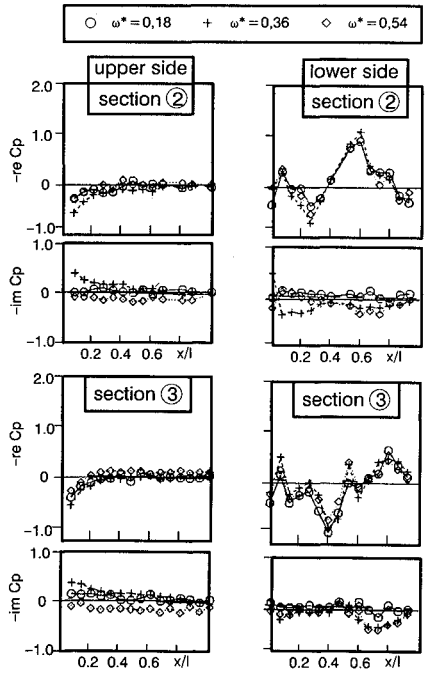

Fig. 14 Unsteady pressure distributions Re $c_p(x/l)$ and Im $c_p(x/l)$ of the wing; influence of ω^*; $M_\infty = 0.18$; $\alpha = 0$ deg; $\zeta_2 = \zeta_5 = 0.34$.

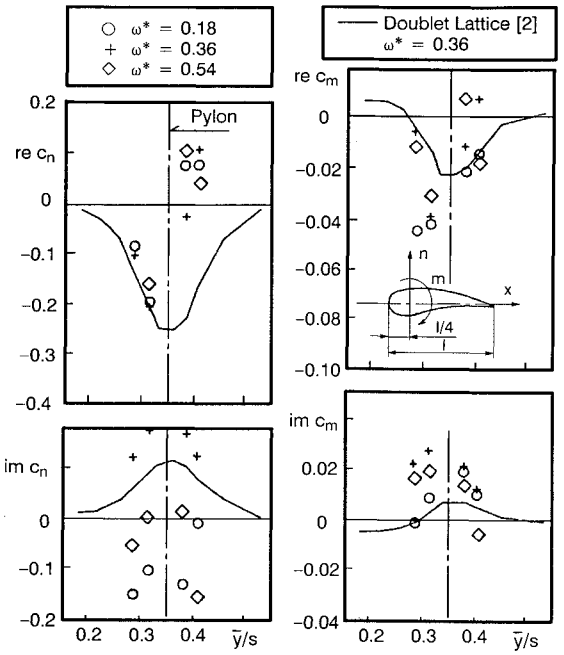

Fig. 15 Unsteady normal force and pitch moment distributions Re $c_n(\bar{y}/s)$, Im $c_n(\bar{y}/s)$, Re $c_m(\bar{y}/s)$, and Im $c_m(\bar{y}/s)$; influence of ω^*; $M_\infty = 0.18$; $\alpha = 0$ deg; $\zeta_2 = \zeta_5 = 0.34$.

pressure distributions is nearly unaffected by ω^* of the engine pitch vibration. Thus, the character of the unsteady pressure distributions is not the result of the harmonically oscillating engine downwash. A local flow separation, which is the reason for the odd unsteady pressure distribution, was found by oil flow visualization at the junction between the wing and pylon.

The integration of the unsteady pressure distributions yields the unsteady local normal force coefficients Re $c_n(\bar{y}/s)$ and Im $c_n(\bar{y}/s)$, and the unsteady local pitch moment coefficients Re $c_m(\bar{y}/s)$ and Im $c_m(\bar{y}/s)$, which are plotted in Fig. 15. The unsteady local normal force and pitch moment coefficients, due to the oscillating engine, are very small and are therefore of minor influence on the unsteady airloads of an oscillating wing. Calculation of the unsteady pressure distribution using the doublet-lattice method cannot, of course, represent the measured unsteady pressures, as shown in Fig. 14. However, the calculated local unsteady airloads are in the same order of magnitude as the measured ones.

Conclusions and Outlook

Experimental investigations of the unsteady airloads on an engine model and a wing/engine combination were carried out. The aim was to find out whether the usually used simplified through-flow nacelles are appropriate as mathematical models in flutter calculations to describe the real flow conditions concerning the engine and the wing/engine combination.

The wind-tunnel tests on the harmonically oscillating isolated engine showed that the pressure distributions are significantly affected by transonic flow, as opposed to the airloads which are nearly unchanged when the Mach number is increased. The unsteady airloads increase with increasing inlet mass flow coefficient and with increasing reduced frequency, whereas the direct influence of the jet strength is small.

The calculated unsteady airloads are smaller than the measured ones at the same inlet mass flow coefficient. This means that the calculated unsteady airloads correspond well with the measurement when the inlet mass flow is throttled, as is the case in the cruise condition of aircraft.

The wind-tunnel tests on the wing/engine model with the engine in harmonic pitch oscillation showed that the unsteady pressures on the wing lower side are strongly affected by flow separation in the region of the wing/pylon junction. The magnitudes of the unsteady airloads are small, and the calculations based on the doublet-lattice method are of the right order.

Finally, it can be concluded that the unsteady airloads of a wing/engine combination are satisfactorily predicted by the usually used doublet-lattice method (as they are necessary for flutter calculations), provided that the engine is of a presently-used type with moderate bypass ratio. Future engine developments will lead to larger engine diameters, so that the influence of the engine aerodynamics on the aircraft flutter behavior will increase. Consequently, the unsteady engine airloads and their interference effects on the wing have to be considered more accurately in the flutter calculations.

Acknowledgment

All results presented in this article have been performed under Contract L-4/86-50067/86 for the German Ministry of Transport.

References

[1]Zimmermann, H., and Vogel, S., "Influence of Main Design Parameters on Flutter Behaviour for Aircraft Configurations with Heavy Concentrated Masses," 56th Meeting of the AGARD Structures and Materials Panel, AGARD CP 354, London, April 1983, *Aeroelastic Considerations in the Preliminary Design of Aircraft*, NATO Advisory Group for Aerospace Research and Development (AGARD), Neuilly-sur-Seine, France, 1983, pp. 6-1–6-11.

[2]Albano, E., and Rodden, W. P., "A Doublet-Lattice Method for Calculating Lift Distributions on Oscillating Surfaces in Subsonic Flow," *AIAA Journal*, Vol. 7, No. 2, 1969, pp. 279–285.

[3]Angelini, J., Chopin, S., and Destuynder, R., "Forces Aérodynamiques Instationnaires Induites par les Vibrations Aéroélastiques d'un Réacteur en Nacelle," *La Recherche Aérospatiale*, No. 4, 1974.

[4]Zingel, H., Vogel, S., Triebstein, H., Schewe, G., and Katzer, E., "Experimentelle und Theoretische Untersuchung der Stationären und Instationären Luftkräfte an Strahltriebwerken," Deutsche Gesellschaft für Luft- und Raumfahrt e.V. (DGLR) Bonn, Jahrestagung 1988, Darmstadt, Germany, 1988; DGLR-Jahrbuch, No. I, Paper 88-059, 1988, pp. 323–332.

[5]Zingel, H., Jajes, U., and Vogel, S., "Bestimmung Instationärer Triebwerksluftkräfte für die Anwendung bei Flatteruntersuchungen," Messerschmitt-Bölkow-Blohm (MBB) Internal Rept., Munich, Germany, TE 234-B27/89, 1989.

[6]Schewe, G., "Beispiele für Kraftmessungen im Windkanal mit Piezoelektrischen Mehrkomponenten-Meßelementen," *Zeitschrift für Flugwissenschaften und Weltraumforschung*, Vol. 14, 1990, pp. 32–37.

[7]Schewe, G., "Force Measurements in Aeroelasticity Using Piezoelectric Multicomponent Transducers," *Proceedings of the International Forum on Aeroelasticity and Structural Dynamics*, Deutsche Gesellschaft für Luft- und Raumfahrt e.V. (DGLR) Bonn, DGLR Rept. 91-06, 1991, pp. 142–149.

[8]Ehrmann, M., Klevenhusen, K. D., Rudolph, K., and Burgsmüller, W., "Computation of Engine-Airframe Interference Flows at Subsonic and Transonic Speed/Comparison with Flight and Wind-tunnel Tests," *International Council of the Aeronautical Sciences (ICAS) Proceedings 1984*, ICAS-84-2.10.1, Toulouse, France, Sept. 1984.